DOI 10.4430/bgo00537

On the reflectance map and the generalised derivative operator

G. Dominici and A. Meloni

Istituto Nazionale di Geofisica e Vulcanologia, Rome, Italy

(Received: 19 December 2025; accepted: 3 July 2026; published online: 4 September 2026)

ABSTRACT The reflectance map is a widely used algorithm in the imaging process to determine the shape of objects. In geophysics, it is also used as a filter to improve the delineation of the edges of buried bodies causing gravimetric or magnetic anomalies. In this paper we recall the theory behind the formulation of the reflectance index and we show that the generalised derivative operator is the result of the reflectance algorithm implementation when applied to a three-dimensional function $f(x,y,z)$. Moreover, we highlight that, in a representation on a horizontal plane, the two are equivalent. We discuss applications of the two filters, introducing the directional derivative, to gravity and magnetic field data and to onshore and offshore total magnetic field anomaly data for Italy.

Key words: magnetic and gravity anomalies, hill shading, reflectance map, directional derivative.

1. Introduction

Hill shading, also called sun shading or shaded relief by some authors, is a commonly used technique when dealing with topographical data (Marston and Jenny, 2015; Jenny and Patterson, 2020). This technique consists of the illumination of a surface and the consequent evaluation of the effects of lights and shadows on that surface (Horn, 1981, 1982). This representation has the advantage of describing the terrain structure accurately up to the spatial limits of the data distribution.

This technique was employed for a long time in a handmade way. Matrix calculus computer applications have extended the use of this technique to geophysical data (Pelton, 1987; Chiappini *et al*., 2000; Golynsky *et al.,* 2002; Cooper, 2003; Bakkali and Amrani, 2007).

In the case of a digital elevation model, which is a bi-dimensional representation of elevation obtained with graphic software, the starting data are the geographical coordinates (x,y) of given points and their altitude as a function of the point location, $z=f(x,y)$. The data need to be homogeneously distributed otherwise, they are arranged to be homogeneously distributed by means of algorithms, such as kriging, minimum curvature, polynomial regression, etc. (Wahba, 1990; Yang *et al*., 2004).

The hill shading process consists of the following steps:

- digital data input;
- computation of reflectance index $R\ (p,q)$;
- map production by processing (merging contour + reflectance map = 3D effect).

© 2026 - The Author(s)

2. The properties of the reflection on surfaces

The reflectance properties of a surface is the ratio of radiance (the amount of light radiating from a surface) to irradiance (the amount of light falling on a surface from a fixed light source). It can be represented as a function of the three angles, *i*, *e*, and *g*, i.e. *F*(*i,e,g*), as defined in Fig. 1 (Horn and Sjoberg, 1979).

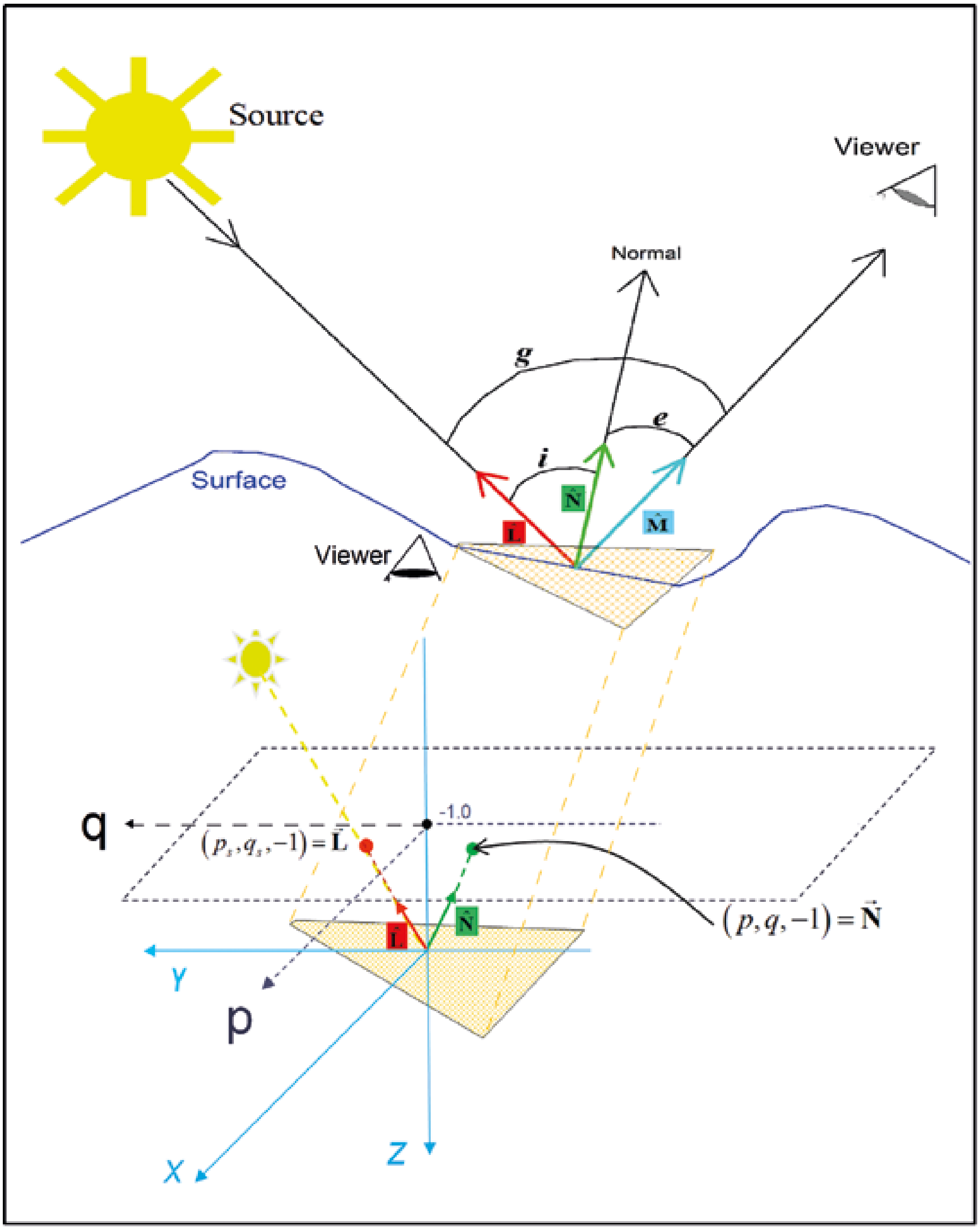

Fig. 1 - Parameters used in text to identify incident and reflected light on a given surface.

The *i* angle is called incident (the angle between the incident ray and the normal to the surface), the *e* angle is called emergent (the angle between the emergent ray and the normal to the surface), and the *g* angle is called phase (the angle between the incident and emergent rays).

In Fig. 1, for an orthographic projection viewed centred, we report *x*- and *y*-axis defined following geographical standards (*x* positive northwards, *y* positive eastwards), and vertical axis *z*, positive downwards.

Moreover:

a) the surface normal vector $\vec{\mathbf{N}}$, can be expressed in terms of surface gradient $(p,q) = (\partial f/\partial x, \partial f/\partial y)$, and coordinates $\vec{\mathbf{N}} = (p,q,-1)$; we work on raster maps and so, for computation of the two gradients $\partial f/\partial x$ and $\partial f/\partial y$, we use a kernel or convolution matrix. In this work, we use the Sobel detector (Shapiro and Stockman; 2001);

b) the $\vec{\mathbf{L}}$, vector, which points in the direction of the light source, with coordinates $\vec{\mathbf{L}} = (p_s,q_s,-1)$ where, in Fig. 2, $p_s = -\cos\phi \tan\vartheta$ and $q_s = -\sin\phi \tan\vartheta$, where ϑ is the polar angle measured from the *z*-axis and ϕ is the azimuth measured anticlockwise from the *x*-axis;

c) the unit vector $\hat{\mathbf{M}}$, which points in the direction of the viewer, with coordinates $\hat{\mathbf{M}} = (0,0,-1)$.

Then, we define:

$$\cos(i) = \frac{1 + pp_s + qq_s}{\sqrt{1+p^2+q^2}\sqrt{1+p_s{}^2+q_s{}^2}} \tag{1}$$

$$\cos(e) = \frac{1}{\sqrt{1+p^2+q^2}} \tag{2}$$

$$\cos(g) = \frac{1}{\sqrt{1+p_s^2+q_s^2}} \tag{3}$$

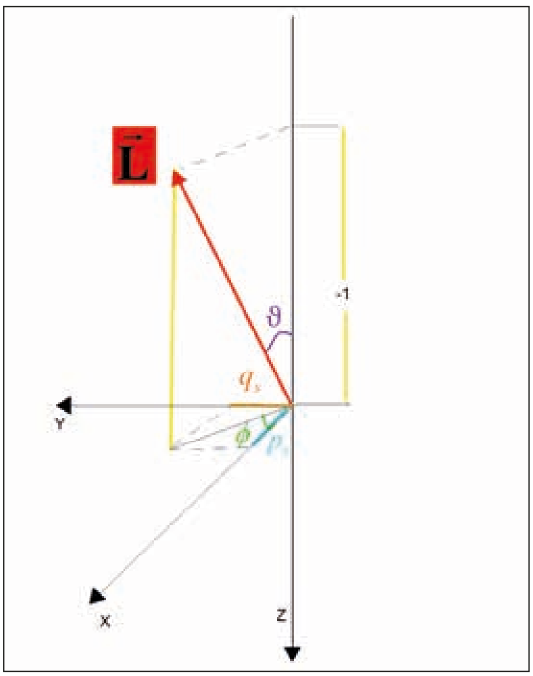

Fig. 2 - Projections of the vector $\vec{\mathbf{L}}$.

Eqs. (1), (2), and (3) are used to transform a surface reflection function, $F(i,e,g)$, into a reflectance $R(p,q)$ map, which determines the proportion of light reflected as a function of p and q.

In an orthographic projection, the viewing direction (and hence the phase angle g) is constant for all the surface elements; thus, for a fixed light source, the reflectance (and hence the viewed image intensity) depends on the surface normal vector.

Usually, a simple approximation is a perfectly diffuse surface, called a Lambertian surface (Koppal, 2014), which appears equally bright from all viewing directions; in this case:

$$F_l(i,e,g) = R(p,q) = I_0 \rho \cos(i) \tag{4}$$

where subscript l is for Lambertian, ρ is the albedo or reflectance factor, and I_0 is the incident light intensity

$$R(p,q) = I_0 \rho \frac{1 + pp_s + qq_s}{\sqrt{1+p^2+q^2}\sqrt{1+p_s^{\,2}+q_s^{\,2}}} = I_0 \rho \frac{\vec{\mathbf{N}} \bullet \vec{\mathbf{L}}}{\left|\vec{\mathbf{N}}\right|\left|\vec{\mathbf{L}}\right|}. \tag{5}$$

Considering that $\left|\vec{\mathbf{L}}\right| = \sqrt{1+p_s^{\,2}+q_s^{\,2}} = \left|\frac{1}{\cos(\vartheta)}\right|$, then, for $-\frac{\pi}{2} \le \vartheta \le +\frac{\pi}{2}$

$$R(p,q) = I_0 \rho \cos(\theta) \frac{1 + pp_s + qq_s}{\sqrt{1+p^2+q^2}} = I_0 \rho \frac{\cos(\vartheta)(1 - \frac{\partial f}{\partial x}\cos\phi \tan\vartheta - \frac{\partial f}{\partial y}\sin\phi \tan\vartheta)}{\sqrt{1 + \left(\frac{\partial f}{\partial x}\right)^2 + \left(\frac{\partial f}{\partial y}\right)^2}}$$

$$= I_0 \rho \frac{\cos(\vartheta)(1 - \frac{\partial f}{\partial x}\cos\phi \frac{\sin\vartheta}{\cos\vartheta} - \frac{\partial f}{\partial y}\sin\phi \frac{\sin\vartheta}{\cos\vartheta})}{\sqrt{1 + \left(\frac{\partial f}{\partial x}\right)^2 + \left(\frac{\partial f}{\partial y}\right)^2}} \tag{6}$$

$$R(p,q) = \frac{\cos\vartheta - \sin\vartheta\left(\frac{\partial f}{\partial x}\cos\phi + \frac{\partial f}{\partial y}\sin\phi\right)}{\sqrt{1 + \left(\frac{\partial f}{\partial x}\right)^2 + \left(\frac{\partial f}{\partial y}\right)^2}}. \tag{7}$$

In Eq. (7) we have not written the values ρ, I_0 as they are, for this work, constants and, hence not relevant for what follows. As can be seen, the brightness does not depend on the viewing direction and it is independent of the angles e and g.

Reflectance varies between -1 (no lighting) and 1 (maximum lighting) with the vector $\vec{\mathbf{N}}$ parallel and towards the vector $\vec{\mathbf{L}}$ source and, when $\vartheta = 0$, we have $0 \le I\,(x,y) \le 1$.

3. From the reflectance map to the directional derivative

Working with the gradients, the reflectance map emphasises the abrupt slope on the surface perpendicularly to the direction chosen by the operator. If we apply it to geophysical data, the enhancement of linear features helps the geological interpretation. However, to the best of our knowledge, few authors have used this type of 'filter' named sunshading (Cooper, 1997, 2002, 2003; Bakkali and Amrani, 2007; Cooper and Cowan, 2007, 2011).

Unfortunately, in all the above-mentioned papers the following equation was used:

$$R(p,q)=\frac{1+pp_s+qq_s}{\sqrt{1+p^2+q^2}+\sqrt{1+p_s^2+q_s^2}}\ . \tag{8}$$

This equation, however, is not so suitable since the denominator reports the sum of the two radicals whereas their product should be reported, as in Eq. (5).

If we now refer to a geophysical potential field, the generic element $H = f(x,y,z)$ (e.g. total magnetic field anomaly or gravimetric anomaly), so $\vec{N}=(\partial f/\partial x\,,\partial f/\partial y\,,\partial f/\partial z)=\nabla f$ is the vector gradient of f. Then, Eq. (7) becomes:

$$R(p,q,r)=\frac{\frac{\partial f}{\partial z}\cos\vartheta-\sin\vartheta\left(\frac{\partial f}{\partial x}\cos\phi+\frac{\partial f}{\partial y}\sin\phi\right)}{\sqrt{\left(\frac{\partial f}{\partial z}\right)^2+\left(\frac{\partial f}{\partial x}\right)^2+\left(\frac{\partial f}{\partial y}\right)^2}}=\frac{\vec{\mathbf{N}}\bullet\vec{\mathbf{L}}}{\left|\vec{\mathbf{N}}\right|\left|\vec{\mathbf{L}}\right|}=\frac{\nabla f\bullet\vec{\mathbf{L}}}{\left|\vec{\mathbf{N}}\right|\left|\vec{\mathbf{L}}\right|}=\frac{D_{\hat{L}}f}{\left|\vec{\mathbf{N}}\right|} \tag{9}$$

considering that $D_{\hat{L}}f=\frac{\nabla f\bullet\vec{\mathbf{L}}}{\left|\vec{\mathbf{L}}\right|}$ is the directional derivative of the element H in the direction of vector $\vec{\mathbf{L}}$.

Finally, Eq. (9) enables us to evaluate the $D_{\hat{L}}f$ normalised with respect to the gradient.

Cooper and Cowan (2011) and Cooper (2018) introduced the generalised derivative operator (*GDO*):

$$GDO=\frac{\left(\frac{\partial f}{\partial x}\sin\varphi+\frac{\partial f}{\partial y}\cos\varphi\right)\cos\delta+\frac{\partial f}{\partial z}\sin\delta}{\sqrt{\left(\frac{\partial f}{\partial z}\right)^2+\left(\frac{\partial f}{\partial x}\right)^2+\left(\frac{\partial f}{\partial y}\right)^2}} \tag{10}$$

where ($\varphi = 270° - \phi$) is the angle in the horizontal plane starting from south and ($\delta = 90° - \vartheta$) is the elevation from the horizontal plane. The authors stated that, when $\delta = 0°$, the *GDO* reduces to:

$$H_x=\frac{\partial\left|A_s\right|}{\partial\left(\frac{\partial f}{\partial x}\right)}=\frac{\frac{\partial f}{\partial x}}{\sqrt{\left(\frac{\partial f}{\partial x}\right)^2+\left(\frac{\partial f}{\partial y}\right)^2+\left(\frac{\partial f}{\partial z}\right)^2}}\quad \text{with } A_s=\sqrt{\left(\frac{\partial f}{\partial x}\right)^2+\left(\frac{\partial f}{\partial y}\right)^2+\left(\frac{\partial f}{\partial z}\right)^2}\,.$$

Indeed, for δ = 0° *GDO* = $\dfrac{\dfrac{\partial f}{\partial x}\sin\varphi + \dfrac{\partial f}{\partial y}\cos\varphi}{\sqrt{\left(\dfrac{\partial f}{\partial z}\right)^2 + \left(\dfrac{\partial f}{\partial x}\right)^2 + \left(\dfrac{\partial f}{\partial y}\right)^2}}$

referring to ϑ and ϕ, Eq. (10) becomes:

$$GDO = \frac{\dfrac{\partial f}{\partial z}\cos\vartheta - \sin\vartheta\left(\dfrac{\partial f}{\partial x}\cos\phi + \dfrac{\partial f}{\partial y}\sin\phi\right)}{\sqrt{\left(\dfrac{\partial f}{\partial z}\right)^2 + \left(\dfrac{\partial f}{\partial x}\right)^2 + \left(\dfrac{\partial f}{\partial y}\right)^2}}. \quad (11)$$

The *GDO* is equal to Eq. (9).

4. Discussion

Figs. 3a and 3b show gravity data for a simple synthetic model, generated using the GRAV_MAG_PRISMA code by Bongiolo *et al*. (2013). This model is identical to the one used by Cooper and Cowan (2011), in their Figs. 1 and 2.

Figs. 3c, 3d, and 3e show the *R(p,q)* in the different directions identifying the surface of the anomaly: the maps are different with respect to the corresponding Figs. 2b, 2d, and 2f by Cooper and Cowan (2011), because the authors used Eq. (8) instead of Eq. (5).

Figs. 3f, 3g, and 3h, shows the *GDO*, computed in the directions specified in the caption, and identify the bodies causing the anomalies, detecting with equal intensity the two prisms.

We note that the application of the two filters generates similar trends.

An image of the element $H = f(x,y,z)$ in the (*x,y*) plane means a representation of *H* at a given level, and, hence, it is difficult if not impossible to represent the $\partial f/\partial z$ on the (*x,y*) plane. So, the image of *R*(*p,q*) and *GDO* (if used at the same level of *z*) have the same characteristics.

In agreement with Cooper and Cowan (2011), when we use *R*(*p,q*) (equal to *GDO*) as a filter we have the advantage "to prevent small features from being dominated by those of larger amplitude" and the disadvantage that "anomalies of both small and large amplitudes show a similar response making geological interpretation of the latter more difficult". To overcome this, together with these filters, $D_{\hat{\iota}} f$, which enables to make numerical evaluations, can be used. The $D_{\hat{\iota}} f$ of Figs. 3i, 3j, and 3k returns a cleaner signal but the intensity is a function of the magnitude of the anomaly and there is the possibility of losing information from weaker signals.

Figs. 4a and 4b show magnetic data from a simple synthetic model (generated using GRAV_MAG_PRISMA code). Figs. 4c, 4d, and 4e show the *R*(*p,q*) in the different directions identifying the surface of the anomaly. Figs. 4f, 4g, and 4h show $D_{\hat{\iota}} f$ and the noise present in *R*(*p,q*) of Figs. 4c, 4d, and 4f is not signified. Figs. 4i, 4j, and 4k represent the same $D_{\hat{\iota}} f$, enlarging the scale for values around zero: this technique emphasises the response to the lower gradient values.

Now, considering a real dataset case, Fig. 5a shows the total intensity magnetic anomaly map of Italy and surrounding marine areas, produced in the year 2000 (Chiappini *et al*., 2000). This map was obtained by merging several ground onshore and offshore datasets gathered during the 1970s and 1980s. Magnetic field diurnal variation was removed and all measurements were

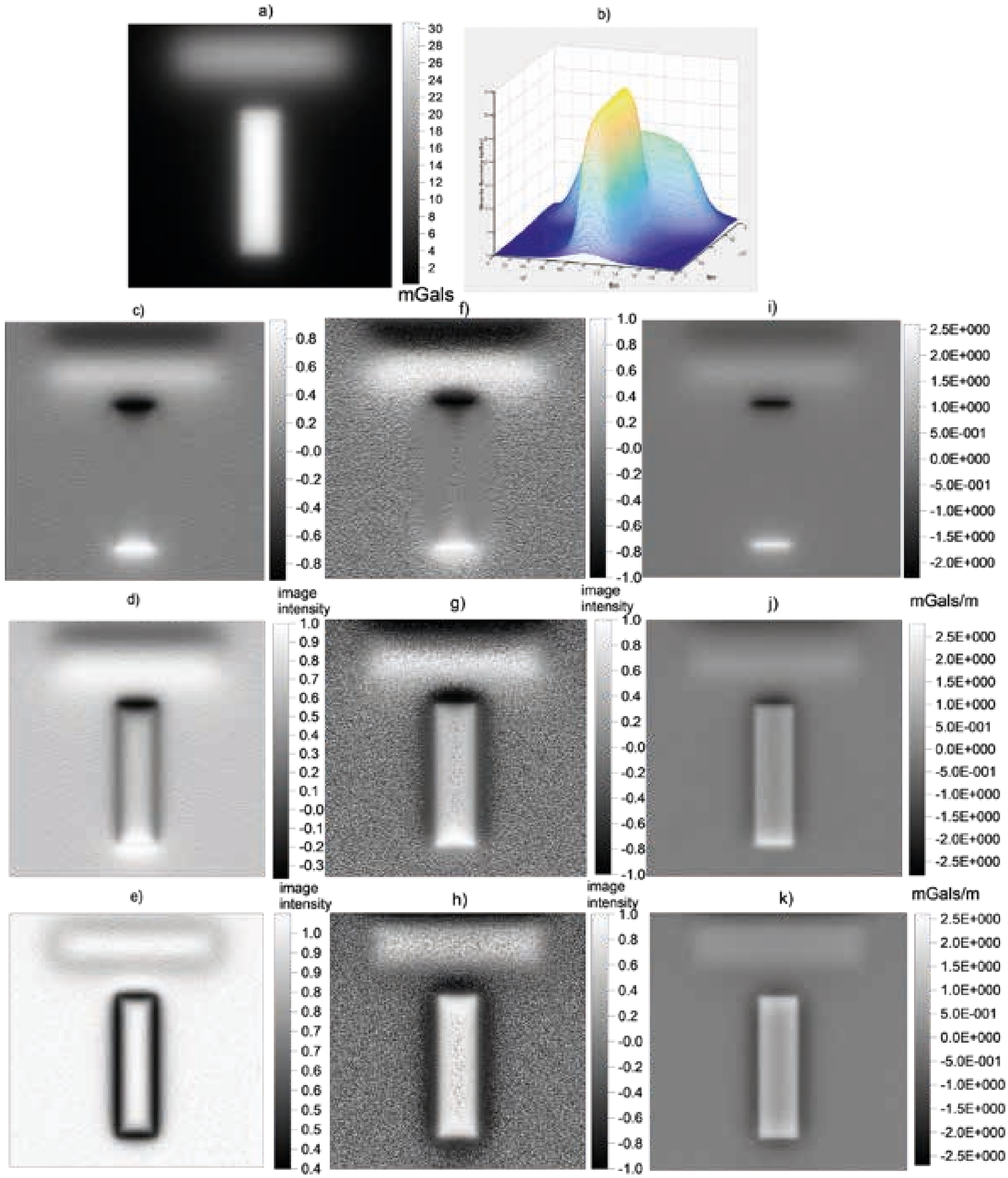

Fig. 3 - a) Gravity model for two rectangular prisms at depths of 12 km (in the north) and 2 km (in the south). Both bodies have a thickness of 10 km and a density contrast of 0.1 g/cm. The dataset is 200 km × 200 km in size. b) 3D view. c) $R(p,q)$ with ϕ = 270° and ϑ = 90°. d) $R(p,q)$ with ϕ = 270° and ϑ = 45°. e) $R(p,q)$ with and ϕ = 270° and ϑ = 0°. f) *GDO* with ϕ = 270° and ϑ = 90° which matches to *GDO* with φ = 0° and δ = 0°. g) *GDO* with ϕ = 270° and ϑ = 45° which matches to *GDO* with φ = 0° and δ = 45°. h) *GDO* with ϕ = 270° and ϑ = 0° which matches to *GDO* with φ = 0° and δ = 90°. i) $D_{\hat{\imath}} f$ with ϕ = 270° and ϑ = 90°. j) $D_{\hat{\imath}} f$ with ϕ = 270° and ϑ = 45°. k) $D_{\hat{\imath}} f$ with ϕ = 270° and ϑ = 0°.

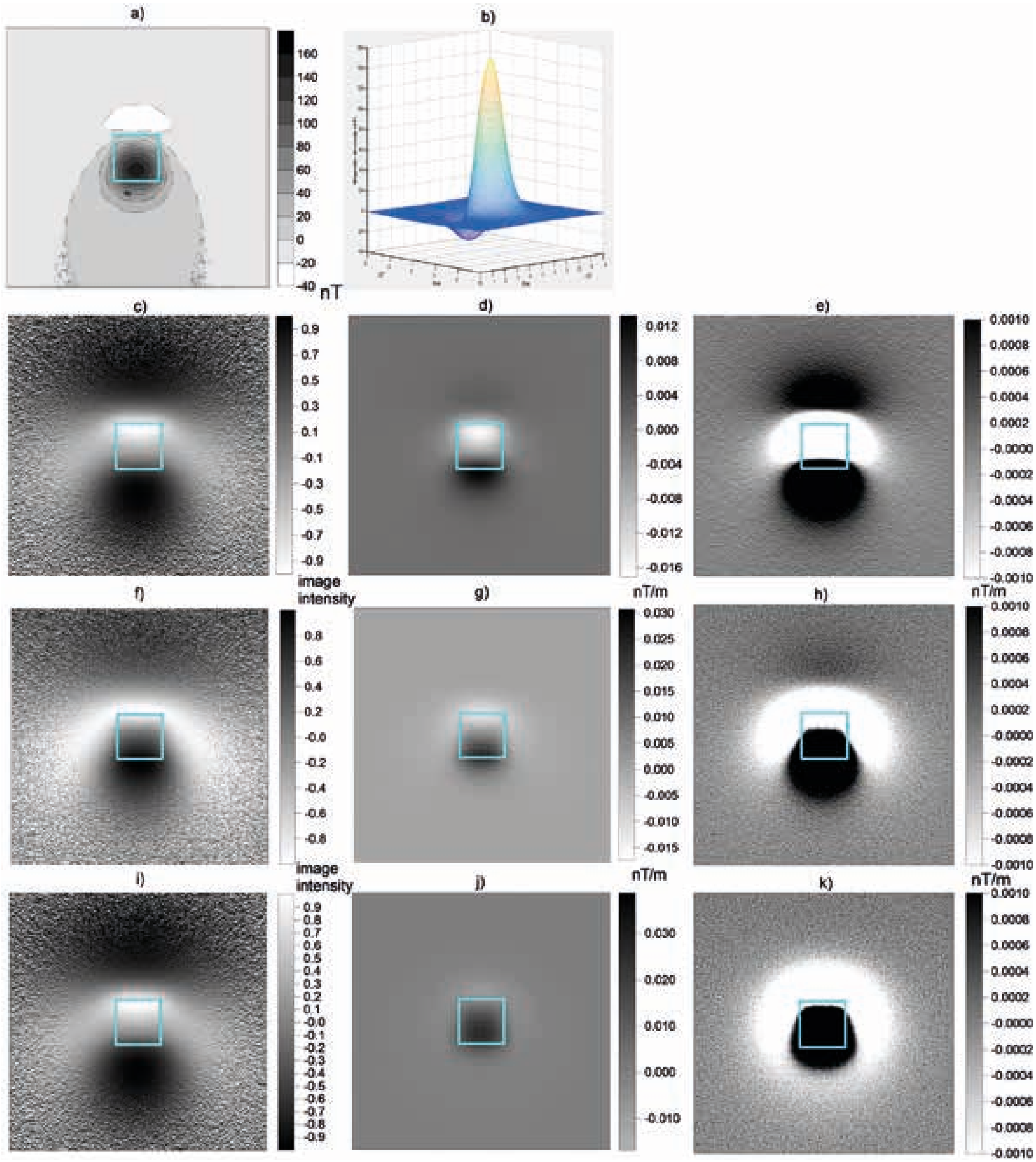

Fig. 4 - a) Synthetic magnetic dataset over a buried prism whose outline is marked with a green square. The dataset is 100 km × 100 km in size and the prism is 16 km side and 7 km deep. The magnetic inclination was 64° and declination was 2° with a total magnetisation for the prism equal to 1.0206 (A/m). Uniformly distributed random noise with an amplitude of 0.1 nT has been added to the data. b) 3D view. c) $R(p,q)$ with ϕ = 270° and ϑ = 90°. d) $R(p,q)$ with ϕ = 270° and ϑ = 45°. e) $R(p,q)$ with ϕ = 270° and ϑ = 0°. f) $D_{\hat{i}} f$ with ϕ = 270° and ϑ = 90°. g) $D_{\hat{i}} f$ with ϕ = 270° and ϑ = 45°. h) $D_{\hat{i}} f$ with ϕ = 270° and ϑ = 0°. i) $D_{\hat{i}} f$ with ϕ = 270° and ϑ = 90° with smaller zero value centred range. j) $D_{\hat{i}} f$ with ϕ = 270° and ϑ = 45° with smaller zero value centred range. k) $D_{\hat{i}} f$ with ϕ = 270° and ϑ = 0° with smaller zero value centred range.

reduced to the geomagnetic epoch 1979.0 and referenced to sea level. The maximum shipborne profile spacing is 10 km offshore and onshore station spacing is between 1 and 10 km. The maximum spacing adopted only in low gradient areas is 10 km.

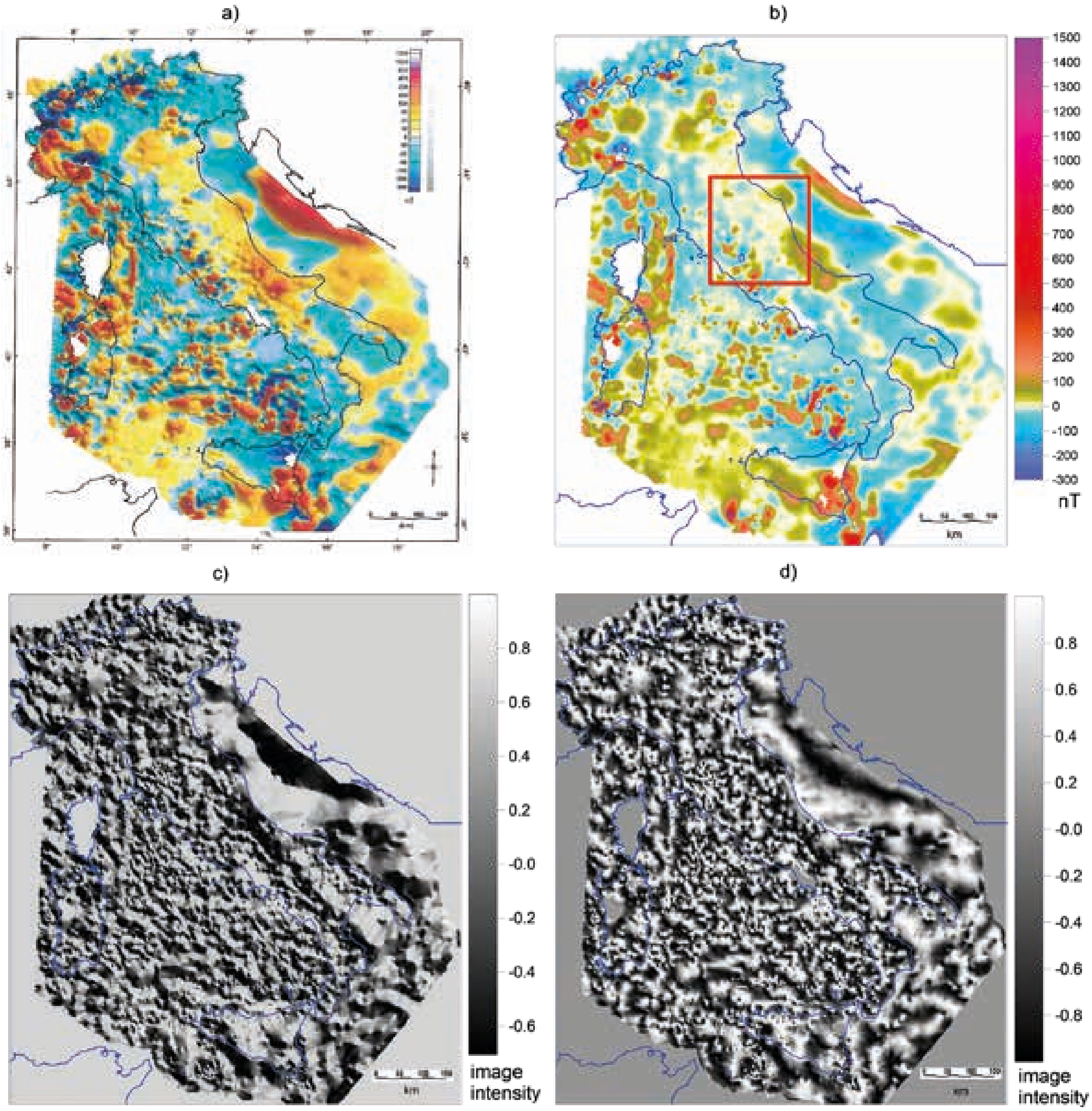

Fig. 5 - a) Magnetic anomaly map of Italy and surrounding marine areas (from Chiappini *et al.*, 2000). b) Pole-reduced magnetic anomaly map. c) $R(p,q)$ with ϕ = 45° and ϑ = 45°. d) *GDO* with ϕ = 45° and ϑ = 45°.

Fig. 5b shows the pole-reduced data (D = 0°, I = 60°). Figs. 5c and 5d show $R(p,q)$ and *GDO* of pole-reduced data for the direction ϑ = 45° and ϕ = 45°. As can be seen, no significant differences appear between the two.

In order to show a smaller scale case, Fig. 6a shows the pole-reduced total intensity magnetic anomaly map referring to the red square area reported in Fig. 5b, which represents the area of central Italy with a northern Apennines fraction.

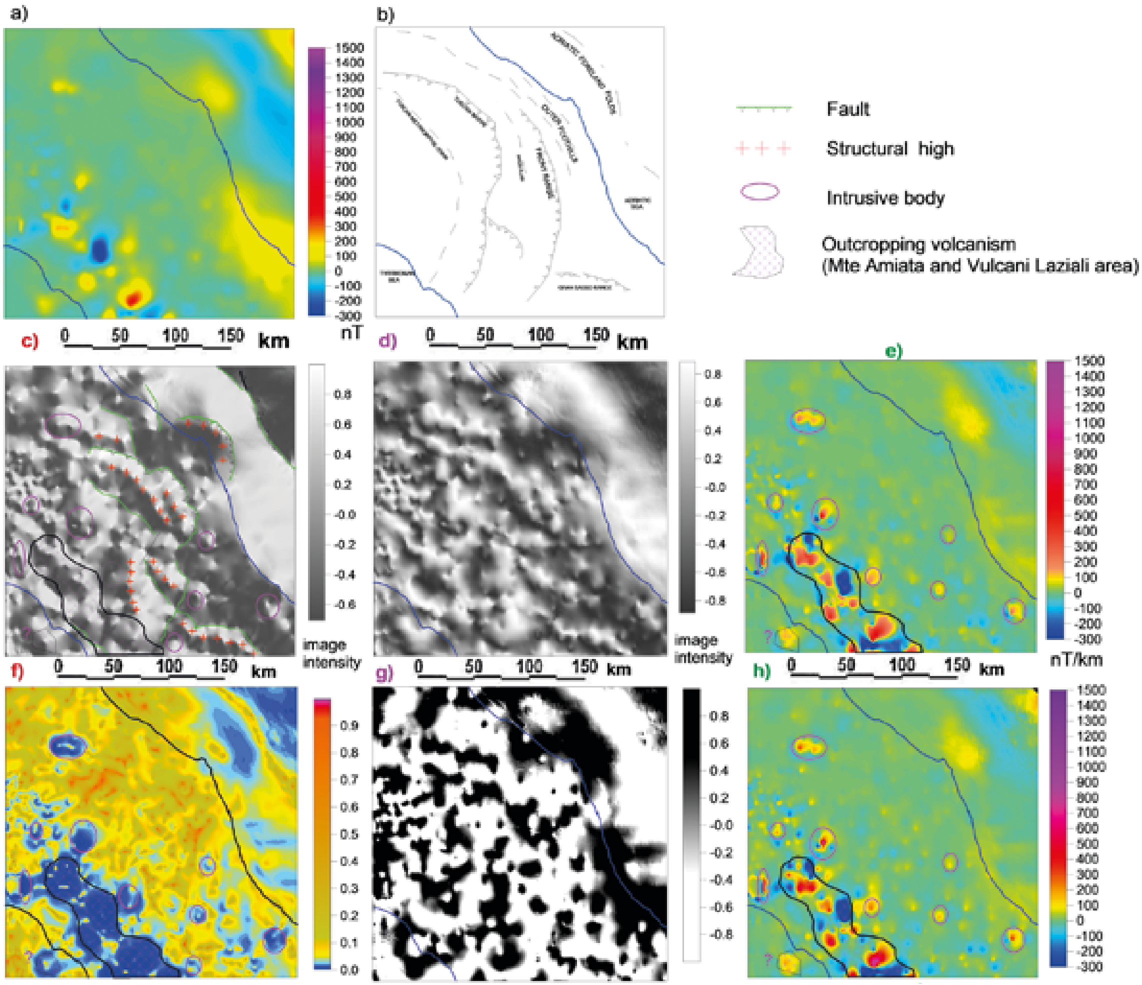

Fig. 6 - a) Pole-reduced anomaly map of the area located by the red square of Fig. 5b and for the same region: b) synthetic structural map, c) $R(p,q)$ map with ϕ = 45° and ϑ = 45°, d) *GDO* map with ϕ = 45° and ϑ = 45°, e) $D_{L} f$ with ϕ = 45° and ϑ = 45°. f) $R(p,q)$ map with ϑ = 0°, g) *GDO* map with ϑ = 0°, h) $D_{L} f$ with ϑ = 0°.

Fig. 6b shows a synthetic structural map of the area of Fig. 6a: the region is characterised by systems of thrusts and folds from Tuscany to Umbria-Marche; the Neogene to Quaternary extensive tectonics to which the main depression of Tuscan-Umbrian basins is attributable dissects this area. Post orogenic volcanic complexes of the Amiata Mountain area and the Latium region volcanoes cut discordantly across all structural units (Bally *et al.*, 1986).

Fig. 6a shows a low amplitude (generally < 30 nT) positive anomaly along the whole external Apennine belt, contrasting with a negative residual field in the adjacent Adriatic foreland areas; in the SW quadrant, i.e. the Tuscan area, the anomalies appear to have short wavelengths of significant intensity, caused by small and shallow sources (typically volcanoes or intrusive bodies).

From Figs. 6c to 6h show the maps by applying the various filters in the directions indicated in the captions, with a possible magnetic interpretation overlaid.

Figs. 6c and 6d show NW-SE structural highs which identify the fronts of the thrust structures and NE-SW discontinuities related to the left lateral strike-slip faults. In the same figures we cannot distinguish the anomalies of the various magmatic complexes with high gradients, well identifiable in Figs. 6e and 6h, as well as in Fig. 6f; in Fig 6g, instead, nothing is detected.

5. Conclusions

Magnetic and gravity anomalies are the difference between observed field strength and the predicted field strength, as observed on the Earth surface, or above it, when flying sensors are used. They respectively reflect variations in local magnetisation due to the presence of magnetic rocks, or density contrasts due to the presence of massive rocks. Both positive and negative values emerge.

For both simple synthetic models and for real datasets *R*(*p,q*) maps show, on different scales, many of the geological and structural elements of selected geographical areas enhancing the respective roles of gravity and magnetic anomalies, that are physically of a different nature indicating their respective anomaly source.

In this paper we have examined some concepts underlying the computation of *R*(*p,q*) and *GDO*, and it was shown that the *R*(*p,q*) is basically the application of the directional derivative. In particular, it was shown that *GDO,* introduced by Cooper and Cowan (2011), seems less efficient as filter with respect to *R*(*p,q*) introducing, for more, an additional noise related to $\frac{\partial f}{\partial z}$. This is clearly shown in Figs. 3 to 6, where *R*(*p,q*) and *GDO* are compared.

R(*p,q*) prevents subtle features from being dominated by those of larger amplitude, while $D_{\hat{L}} f$, the directional derivative with respect to the vector $\vec{\mathbf{L}}$, taking into consideration the maximum and minimum values of the gradient, will be less affected by the noise and enable us to compute the value of the gradient in the various directions.

After all, when geophysical data are represented with the *GDO* filter on an (*x,y*) plane, no effect from $\frac{\partial f}{\partial z}$ can be seen and so we might as well filter the data with *R*(*p,q*).

A different matter is when we consider numerical evaluations: in this case, in fact, it seems more convenient to work with directional derivatives $D_{\hat{L}} f$.

REFERENCES

Bakkali S. and Amrani M.; 2007: *Analyzing the enhancement edges of the Bouguer gravity anomaly map using sunshading method (area of the Tangier-Tetuan, Morocco)*. Revista Facultad de Ingenieria, Universidad de Antioquia, 39, 69-78.

Bally A.W., Burbi L., Cooper C. and Ghelardoni R.; 1986: *Balanced sections and seismic reflection profiles across the central Apennines*. Mem. Soc. Geol. It., 35, 257-310.

Bongiolo A.B.S., De Souza J., Ferreira F.J.F. and De Castro L.G; 2013: *GRAV MAG PRISM: a Matlab/Octave program to generate gravity and magnetic anomalies due to rectangular prismatic bodies*. Revista Brasileira de Geofisica, 31, 347–363.

Chiappini M., Meloni A., Boschi E., Faggioni O., Beverini N., Carmisciano C. and Marson I.; 2000: *Shaded relief magnetic anomaly map of Italy and surrounding marine areas*. Annali di Geofisica, 43, 983-989.

Cooper G.R.J.; 1997: *GravMap and PFproc: Software for filtering geophysical Map Data*. Computer and Geosciences, 23, 91-101.

Cooper G.R.J.; 2002: *Fixed point inversion of geophysical data*. Computer and Geosciences, 28, 799-808.

Cooper G.R.J.; 2003: *Feature detection using sun shading*. Computer and Geosciences, 29, 941-948.

Cooper G.R.J.; 2018: *The Interpretation of the Generalized Derivative Operator*. Geophysical Prospecting, 66(1), 197–206, doi: 10.1111/1365-2478.12539.

Cooper G.R.J. and Cowan D.R.; 2007: *Enhancing linear features in image data using horizontal orthogonal gradient ratios*. Computer and Geosciences, 33, 981-984.

Cooper G.R.J. and Cowan D.R.; 2011: *A generalized derivative operator for potential field data*. Geophysical Prospecting, 59, 188-194.

Golynsky A.V., Alyavdin S.V., Masolov V.N., Tscherinov A.S. and Volnukhin V.S.; 2002: *The composite magnetic anomaly map of the East Antarctic*, Tectonophysics, 347, 109-120.

Horn B.K.P.; 1981: *Hill shading and reflectance map*. Proceedings of IEEE, 69, 13-47.

Horn B.K.P.; 1982: *Hill shading and the reflectance map*. Geo-Processing, 2, 65–146.

Horn B.K.P. and Sjoberg R.W.; 1979: *Calculating the reflectance map*. Applied Optics, 18, 1770-1778.

Jenny B and Patterson T.; 2020: *Aerial perspective for shaded relief*. Cartography and Geographic Information Science, 48(1), 21–28, doi: 10.1080/15230406.2020.1813052.

Koppal S.J.; 2014: *Lambertian reflectance*. In: Ikeuchi K. (ed), Computer Vision, Springer, Cham, Switzerland, pp. 441–443, doi: 10.1007/978-3-030-03243-2_534-1.

Marston B.E. and Jenny B.; 2015*: Improving the representation of major landforms in analytical relief shading*. Int. J. Geographical Information Science, 29(7), 1144–1165, doi: 10.1080/13658816.2015.1009911.

Pelton C.A.; 1987: *Computer program for hill-shading digital topographic data sets*. Computers & Geosciences, 13, 545-548.

Shapiro L.G. and Stockman G.C.; 2001: *Computer Vision*. Prentice Hall, Upper Saddle River, NJ, USA, 580 pp.

Wahba G.; 1990: *Spline models for observational data*. Society for Industrial and Applied Mathematics, Philadelphia, PA, USA, 161 pp., doi: 10.1137/1.9781611970128.

Yang C.S., Kao S.P., Lee F.B. and Hung P.S.; 2004: *Twelve different interpolation methods: A case study of Surfer 8.0*. In: Proceedings of the 20th ISPRS Congress, 35, pp. 778-785, http://www.cartesia.org/geodoc/isprs2004/comm2/papers/231.pdf.

Corresponding author: Guido Dominici
Istituto Nazionale di Geofisica e Vulcanologia
Via di Vigna Murata 605, 00143 Roma, Italy
Phone: +39 06 518601; e-mail: guido.dominici@ingv.it